This is a preproof accepted article for *Mineralogical Magazine*
This version may be subject to change during the production process
DOI: 10.1180/mgm.2025.10155

Crystallography of oriented magnetite inclusions in apatite

Xingtong Li [1], Chang Xu [2], Jinyu Zheng [2], Hongtao Shen [3], Andy H Shen [1], Qian Zhang [1]*

1. Gemmological Institute, China University of Geosciences, Wuhan 430074, China

2. School of Earth Science, China University of Geosciences, Wuhan 430074, China

3. State Key Laboratory of Geological Processes and Mineral Resources, China University of Geosciences, Wuhan 430074, China

* Correspondence: qianzhang@cug.edu.cn

Abstract

In this study, natural apatite containing fine-grained magnetite inclusions with well-developed shape-preferred orientation is investigated. These inclusions are aligned in trails parallel to the hexagonal prism facets and elongated along the c-axis of apatite. Electron probe microanalysis (EPMA) reveals a chemically homogeneous apatite, while Energy dispersive X-ray spectroscopy (EDS) and Raman spectroscopy identify these inclusions as magnetite. Carbonate-bearing inclusions, including calcite and gas-liquid inclusions with CO_2, N_2, and dissolved carbonate ions, are also observed. Calcite inclusions likely indicate carbonatitic magma during apatite growth, whereas gas-liquid inclusions suggest later hydrothermal alteration. Optical microscopy reveals three shape-preferred orientation (SPO) groups of lamellar magnetite inclusions, each elongated parallel to $<0001>_{Ap}$ and to one of the three $<11\bar{2}0>_{Ap}$ directions. Electron backscatter diffraction (EBSD) analysis defines a consistent axial relationship of $<0001>_{Ap}//<110>_{Mag}$ across all inclusions. Additionally, inclusions following the three SPO directions exhibit distinct but symmetrically related planar relationships, reflecting two specific crystallographic orientation relationships (CORs). COR-1: one of the $\{11\bar{2}0\}_{Ap}$ planes parallel to one of the $\{411\}_{Mag}$ planes, and one of the $\{10\bar{1}0\}_{Ap}$ planes parallel to one of the $\{211\}_{Mag}$ planes. This COR is expressed in direction 1 and 3 as two equivalent variants. COR-2: one of the $\{11\bar{2}0\}_{Ap}$ planes parallel to one of the $\{211\}_{Mag}$ planes, and one of the $\{10\bar{1}0\}_{Ap}$ planes parallel to one of the $\{411\}_{Mag}$ planes.

These orientation patterns suggest variant selection during 2D interface-controlled nucleation, likely governed by the symmetry and surface geometry of the apatite host. The crystallographic relationships and the surface features of apatite suggest a secondary origin for magnetite, where Fe was introduced through etch pits on the (0001) facet and nucleated along dislocations in crystal channels or pits. The hexagonal morphology of magnetite inclusions reflect the crystallographic control by apatite symmetry. We suggest that a fluid-induced dissolution-recrystallization process produces the hex-like morphologies of magnetite inclusions and facilitates their incorporation into the host. The necking-down of fluid inclusions further support this process.

Keywords: oriented inclusions, shape-preferred orientation, crystallographic orientation relationships, apatite, magnetite

Introduction

Mineral inclusions are recognized as essential carriers of geological and petrogenetic information, such as paleomagnetic transformations and metamorphic events experienced by the host minerals. The properties and chemical composition of inclusions are closely associated with the rock history and, in some cases, can be used to infer the pressure-temperature conditions during the host mineral formation (Ashley *et al.*, 2015). Shape-preferred oriented inclusions are commonly seen, often presenting as needle or lamella shapes elongated parallel to one or several crystallographic directions of the host crystal. Various shape-oriented inclusion-host pairs have been studied, such as oriented rutile inclusions in corundum (Palke and Breeding, 2017) or garnet (Hwang *et al.*, 2015); oriented iron oxides in feldspar (Jin *et al.*, 2022) and pyroxene (Feinberg *et al.*, 2004); and oriented ilmenite in magnetite (Tan *et al.*, 2016) and amphibole (Xu *et al.*, 2020).

Although most inclusion studies focus on geological implications, shape-oriented inclusions can also contribute to the aesthetic of gemstones. Rough crystals containing abundant shape-oriented inclusions or parallel fine channels can display distinct optical effects, such as chatoyancy and asterism, after directional polishing. Numerous gemstones are known to exhibit these effects, ranging from commonly studied varieties such as corundum, chrysoberyl, and garnet, to rarer minerals including beryl, tourmaline, quartz, etc. (Schmetzer

https://doi.org/10.1180/mgm.2025.10155 Published online by Cambridge University Press

et al., 2002; Schmetzer *et al.*, 2004; Schmetzer *et al.*, 2016; Yu *et al.*, 2019). The arrangement and orientation of inclusions determine whether the gemstone exhibits asterism or chatoyancy. Therefore, research into oriented inclusions holds value in mineralogical, geological, and gemological contexts.

The potential growth mechanisms of oriented inclusions are inherently complex, involving not only the distinct chemical compositions of host and inclusion phases but also their crystal structures and mutual crystallographic relationships. Geochemical data from inclusions can reflect the composition and evolution of the crystallizing fluid, while crystallographic relationships provide constraints on the space and time of inclusion formation. For example, the formation of oriented monazite inclusions in apatite, which consumed rare earth elements (REEs) from the host apatite, has been interpreted as a product of fluid-assistant dissolution-reprecipitation replacement reactions (Harlov *et al.*, 2002; Harlov *et al.*, 2005). Information about inclusion shape, spatial distribution, and the orientation relationships such as shape orientation relationship (SOR) and CORs, is widely recognized as fundamental to understanding inclusion formation mechanisms (Habler and Griffiths, 2017). When inclusions of a single phase present within a host exhibit consistent SORs, a unified SPO is typically observed. CORs, which describe systematic misorientations between neighboring crystals, can provide insight into whether inclusions formed via two-dimensional (2D) interface controlled nucleated on a single surface of the host or under three-dimensional (3D) volumetric control, involving nucleation within the host and orientation control by simultaneous interaction of multiple sets of planes (Habler and Griffiths, 2017; Kohn *et al.*, 2024). However, CORs alone are often insufficient to definitively determine contact geometry or inclusion origin. Detailed interpretation generally requires large spatially resolved datasets that capture variation in multiple parameters across microstructural domains, e.g. (Kohn *et al.*, 2024).

In some cases, inclusions of a single phase occur with multiple crystallographic orientations relative to the host, leading to a variety of CORs. However, not all these relationships reflect specific, fixed lattice alignments. Alternatively, some inclusions may exhibit statistical CORs (also termed non-specific CORs), characterized by a certain freedom of misorientation between the inclusion and host lattices (Griffiths *et al.*, 2016). To

https://doi.org/10.1180/mgm.2025.10155 Published online by Cambridge University Press

distinguish between specific and statistical CORs, and to assess their representativeness within a given system, a sufficiently large and representative number of inclusions must be analyzed. Using EBSD, large COR datasets can be acquired. When combined with transmission electron microscopy (TEM), detailed analysis of angular misorientations and interface structures of a specific host-inclusion pair becomes possible. Together, these analytical methods are widely applied to investigate inclusion growth mechanisms and their relation to rock-forming conditions (Feinberg *et al.*, 2004; Proyer *et al.*, 2013; Britton *et al.*, 2016; Griffiths *et al.*, 2016; Habler and Griffiths, 2017; Keller and Ague, 2019; Griffiths *et al.*, 2020; Ageeva *et al.*, 2022; Kohn *et al.*, 2024).

Recently, some interesting apatite specimens with shape-preferred oriented inclusions have been found in the secondary deposit in Madagascar, exhibiting a pronounced chatoyancy following directional cutting and polishing. In hand specimen, the apatite appears greyish-yellow and contains abundant, lath-shaped inclusions that display metallic luster under reflected light. Apatite frequently exhibits chatoyancy, and some African countries, such as Madagascar, Tanzania, Kenya, and Namibia, are notable sources of chatoyant and asteriated apatite (Barot *et al.*, 1995; Johnson, 2014). India, Myanmar, and Sri Lanka also reported occurrences of similar materials (Mauthner and Ottaway, 2015). The chatoyant effect in apatite is generally attributed to inclusions with shape-preferred orientation, previously identified as goethite or Fe-bearing inclusions from the Taita Mountains in Kenya (Barot *et al.*, 1995), and the Darren mine located near Ambilobé in the Vohemar District of northern Madagascar (Rakovan and Laurs, 2016), parallel growth tubes (Kammerling *et al.*, 1995), or short, fibrous white inclusions from Madagascar (Kammerling and Koivula, 1990; Barot *et al.*, 1995; Kammerling *et al.*, 1995; Rakovan and Laurs, 2016). Moreover, monazite, dolomite, hematite, magnetite, pyrrhotite and triphylite inclusions elongated along the the c-axis of the host have also been reported in apatite (Zhang and Liou, 1999; Harlov *et al.*, 2002; Sun *et al.*, 2007; Broska *et al.*, 2014; Kurylo *et al.*, 2025).

While previous studies have focused on the phase, compositions, and P-T formation conditions of inclusions in apatite (Broska *et al.*, 2014; Rakovan and Laurs, 2016), relatively little literature exists regarding either the crystallographic orientation relationships between inclusions and the apatite host, or their potential to document the crystallization history of

https://doi.org/10.1180/mgm.2025.10155 Published online by Cambridge University Press

either phase. In this study, these unusual apatite specimens from Madagascar are analyzed using EBSD to determine crystallographic relationships between inclusions and host. Additionally, EPMA and EDS mapping are used to investigate the chemical composition, and Raman spectroscopy used to identify the phases. These results contribute to understanding the growth mechanisms of oriented inclusions in apatite and provide some insights relevant to other gemstones exhibiting similar optical features.

Materials and methods

Euhedral apatite samples have been collected from a mineral dealer, who claimed they were sourced from the secondary deposit in Madagascar. Photos of apatite samples were taken by a Nikon D810 camera and Leica DFC 550-M205-A microphotographic system at the Gemmological Institute of China University of Geoscience (Wuhan).

Two thin sections were sliced from apatite A1 and A2 and named TS-1 and TS-2, respectively. TS-1 is cut nearly parallel to the visible basal pinacoid of sample A1, and TS-2 is cut nearly parallel to one of the visible hexagonal prism facets of sample A2. The sections were polished for EPMA, EDS, and EBSD analysis. First, a series of diamond powders with decreasing grain-size from 1 μm, 0.5 μm, 0.25 μm to 0.05 μm were used for preliminary polishing, each step was around 20 minutes; later, they were polished in a vibratory polisher for approximately eight hours with 0.05 μm silica polishing solution to remove defects more effectively. Optical observation and microphotography were conducted on a Zeiss Axioscope A1 polarizing microscope at the Advanced Microscope Laboratory of the School of Earth Science, China University of Geosciences (Wuhan).

Major element compositions of the apatite were conducted at Wuhan Sample Solution Analytical Technology Co., Ltd., Wuhan, China, using a JEOL JXA-8230 EPMA. The analysis was performed with an accelerating voltage of 15 kV, an electron probe current of 10 nA, and a defocused beam of 5 μm. The peak counting time was 10 seconds on element peaks and 5 seconds on background for each element. The following mineral standards were used: quartz (Si); olivine (Mg); magnetite (Fe); rhodonite (Mn); apatite (Ca); jadeite (Na); apatite (P); celestite (Sr); barite (S); monazite (Nd, Ce and La); tugtupite (Cl); apatite (F). These elements were measured by the WDS crystals: PETJ (Ca, La and Ce), TAP (Na, Mg, Si, and

https://doi.org/10.1180/mgm.2025.10155 Published online by Cambridge University Press

Sr), LIFH (Nd, Mn, and Fe), PETH (Cl, S, and P) and LDE1 for F. The detection limits for each element were approximately: 221.13 ppm for Ca, 598.13 ppm for La, 582.00 ppm for Ce, 200.38 ppm for Na, 139.75 ppm for Mg, 196.38 ppm for Si, 334.00 ppm for Sr, 451.50 ppm for Nd, 253.13 ppm for Mn, 271.38 ppm for Fe, 530.25 ppm for F, 76.25 ppm for Cl, 183.00 ppm for S, 213.75 ppm for P, and 384.13 ppm for Y.

The Raman spectra of inclusions within apatite were acquired on sample TS-2 using a Jasco NRS7500 Raman spectrometer at the Gemmological Institute of China University of Geosciences (Wuhan), with the following parameters: 457 nm excitation wavelength, a 12.7 mW laser power, and 1800 grooves/mm grating. The wavenumber was calibrated by testing a silicon single-crystal wafer before conducting all measurements. All spectra were obtained at room temperature.

Backscattered electron (BSE) imaging and EDS analysis were carried out on a Thermo Fisher Helios G4 double-beam scanning electron microscope (SEM) equipped with Oxford Instruments EDS detector with UltimMax 100 (100 mm^2 sensor size) in the State Key Laboratory of Geological Process and Mineral Resources, in China University of Geosciences (Wuhan). The accelerating voltage, working distance and beam current were set to 15 Kv, 10 mm and 1.6 nA, respectively. The samples were coated before the analysis to avoid charging in the SEM. EDS analysis were conducted in mapping mode to investigate the two-dimensional distributions of Ca, P, O, Fe, Mg, Al and Ti.

EBSD analysis was carried out on a Zeiss Sigma 300VP SEM equipped with an Oxford Instruments Aztec Symmetry EBSD detector at the SEM-EBSD laboratory, School of Earth Sciences, China University of Geosciences (Wuhan). Working conditions were as follows: 70° sample tilt angle, 20 kV accelerating voltage, 19.5 mm working distance, 120 μm aperture size and low-vacuum mode. The thin sections were uncoated. Since the SEM used a fixed aperture and did not display the beam current, the beam current is approximately 15 nA. To acquire the whole orientation imaging data for each chosen exposed section of inclusion, the mapping mode was used for the EBSD analysis. Diffraction patterns were collected with the map size of 622×512 pixels and the step size of 0.3-0.5 μm.

The EBSPs of apatite were indexed by using the crystal structure with space group $P6_3/m$, a = 9.4052 Å, c = 6.9125 Å (Hughes *et al.*, 1991). The EBSP of magnetite were

https://doi.org/10.1180/mgm.2025.10155 Published online by Cambridge University Press

indexed by using the crystal structure with space group $F\bar{3}dm$, a = 8.3958 Å (Wechsler *et al.*, 1984). The Oxford Instruments AztecCrystal software was used for data processing and producing pole figures of indexed crystals. All pole figures are plotted as upper-hemisphere stereographic projections. To ensure data quality, only those measurements with mean angular deviation (MAD) values below 1° were accepted for analysis. Data points misoriented by more than 5° were removed based on comparisons with all eight neighboring measurements. During orientation map reconstruction, non-indexed points were replaced with the most common orientation among their neighbors to minimize artefacts.

Results

The features of apatite host and inclusions

The natural color of the studied apatite is light greenish-yellow, the translucent and greyish appearance results from the presence of numerous dark inclusions (Fig. 1a). The two studied apatite samples are euhedral crystals that exhibit relatively similar internal features (Fig. 1b). Sample A1 consists of a combination of basal pinacoid, hexagonal prism and hexagonal bipyramid. The fragmentary sample A2 preserves only unbroken hexagonal prism facets and a small hexagonal bipyramid facet. Owing to the moderate Mohs hardness of apatite, the crystal edges were worn to different degrees.

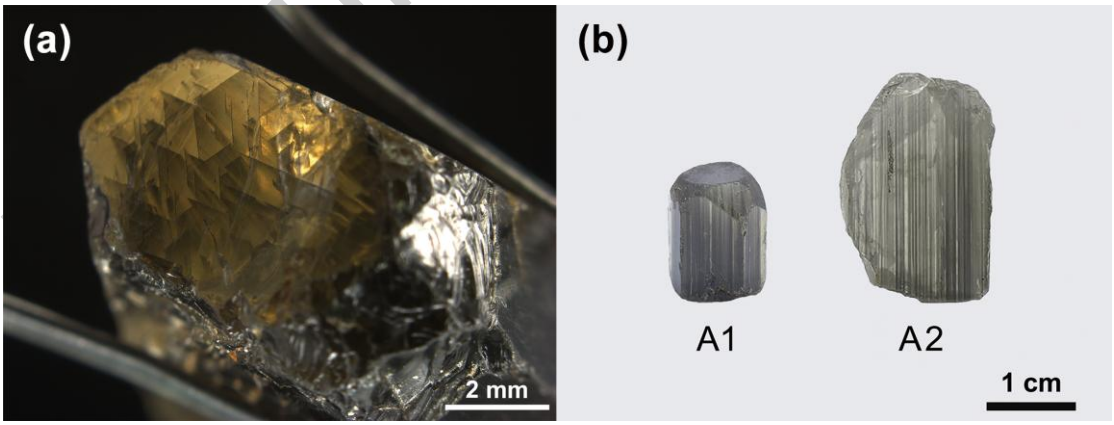

Fig. 1. (**a**) Dark shape-oriented inclusions cross-cut with each other observed through the basal pinacoid of euhedral apatite. (**b**) Two euhedral apatite samples appear densely striped, due to the presence of evenly distributed, long and straight lath-shaped inclusions.

As observed through the basal pinacoid of apatite sample A1, dark inclusion trails are regularly oriented in three directions, parallel to the traces of the hexagonal prism facets of

https://doi.org/10.1180/mgm.2025.10155 Published online by Cambridge University Press

apatite (Fig. 1a). In thin section TS-1, these trails of the inclusions are observed to intersect at angles of 60° and 120° (Fig. 2a). High-magnification optical images reveal that each trail comprises numerous thin, discontinuous lamellae (Fig. 2b), ranging from 5 to several hundred μm in length and 2-10 μm in width. In thin section TS-2, inclusions are observed to be strongly elongated parallel to the c-axis of apatite, indicating well-developed shape-preferred orientation related to the host crystal (Fig. 2c). Based on observations from both thin sections, lath-shaped inclusions that form three distinct shape preferred orientations groups. Each SPO group is characterized by elongated directions that are simultaneously parallel to the apatite c-axis and parallel to one of the <11$\bar{2}$0> crystallographic directions. This dual alignment indicates a systematic relationship between inclusion morphology and host crystal lattice geometry.

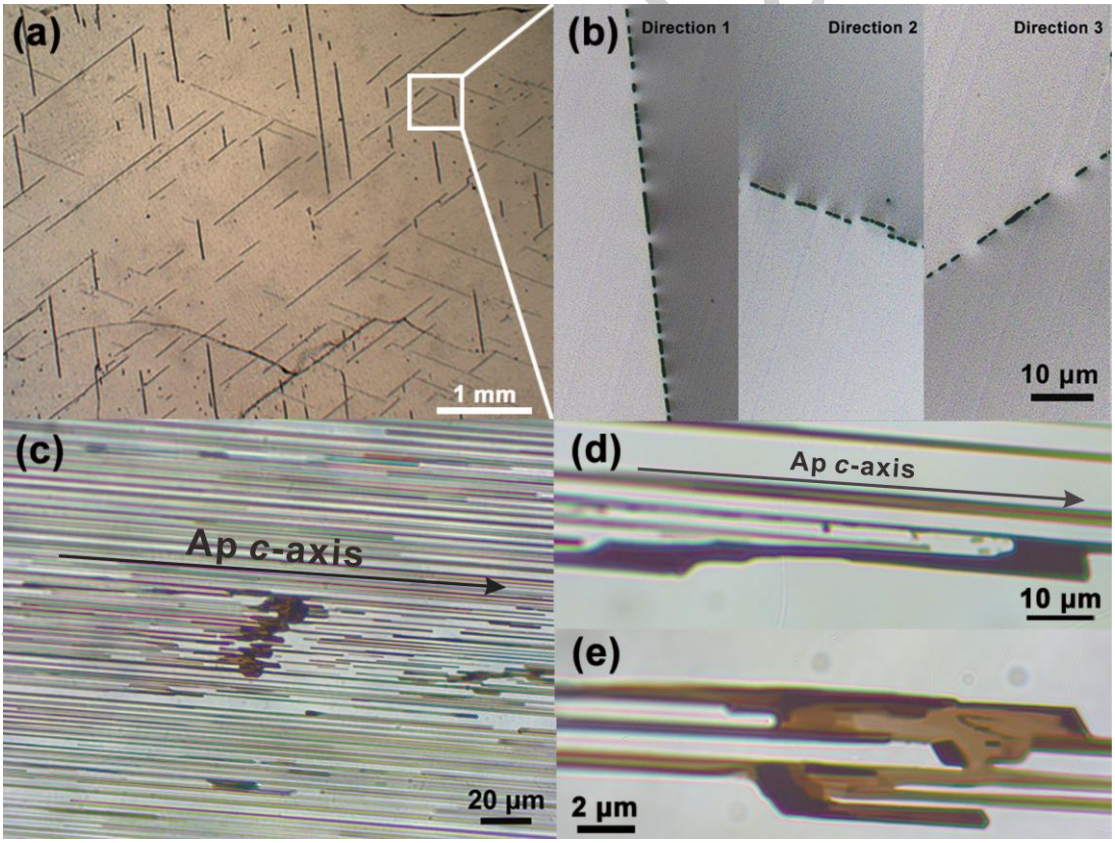

Fig. 2. Photomicrographs of the inclusions under transmitted light. (**a**) In thin section nearly parallel to the basal pinacoid of apatite A1, inclusions trails show three preferred orientations. (**b**) Magnification of the white square of Fig. 2a, showing trail composed of several discontinuous lamellas. (**c**) Thin section nearly parallel to the hexagonal prism facets of apatite A2. The c-axis direction of apatite is marked on the fig. 2c (same for Fig. 2d and e). (**d, e**) Magnified observation showing dark inclusions not completely separated. The darkened and smooth edges observed in Fig. 2d may indicate that the inclusions were being dissolved.

https://doi.org/10.1180/mgm.2025.10155 Published online by Cambridge University Press

In addition to the dark lath-shaped inclusions, several other types of inclusions exist within the apatite. Prism-shaped crystal inclusions extending along the c-axis of apatite were observed (Fig. 3a, e). Multiple gas-liquid two-phase inclusions with different sizes extended along the *c*-axis of apatite are observed, most of them display a necking-down appearance. (Fig. 3b, c). Some faceted crystal inclusions without clear shape-preferred orientation were also found (Fig. 3d).

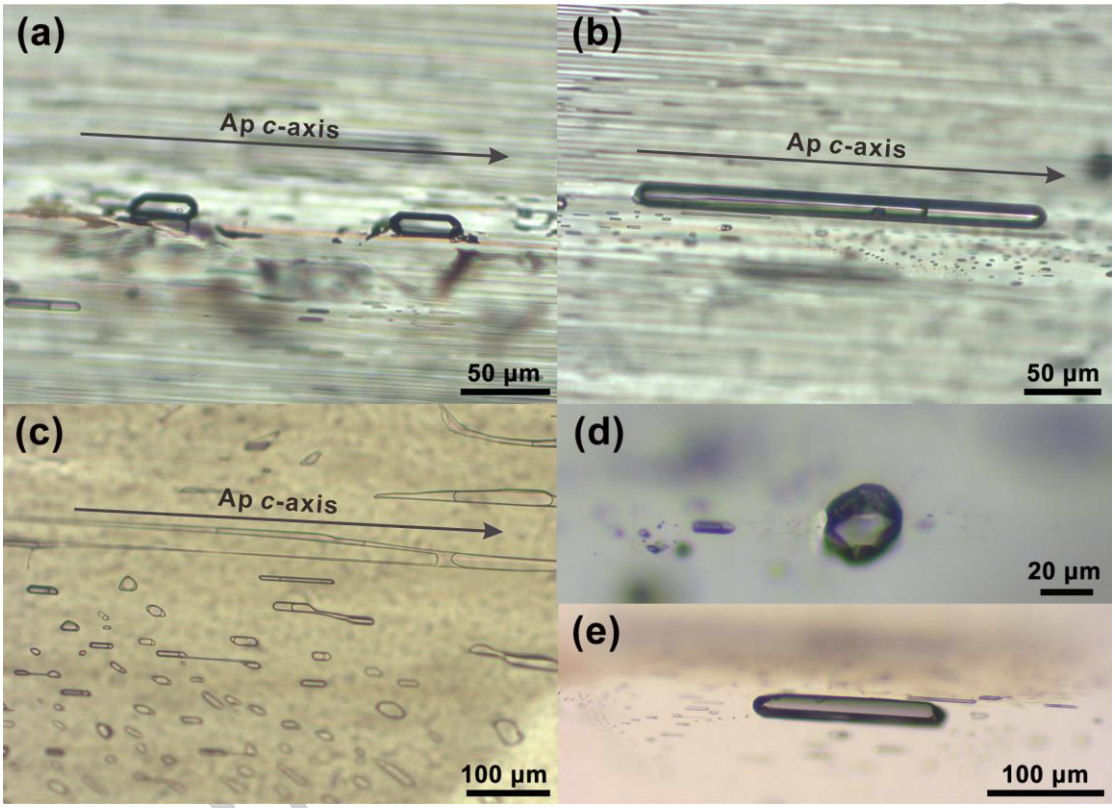

Fig. 3. Typical inclusions observed within thin section sample TS-2. (**a**) Prism-shaped crystal inclusions are crystallographically aligned to the apatite host. (**b**) Tubular inclusion composed of gas and liquid phases. (**c**) Abundant gas-liquid two-phase inclusions elongated along the apatite c-axis, some of them showing distinct necking-down effects. (**d**) Faceted crystal inclusion. (**e**) Another prism-shaped crystal inclusions elongated along the c-axis of the apatite host.

Chemical compositions

The major composition of the apatite is measured along core-to-rim profiles using EPMA (Table 1). EPMA results indicate a homogeneous overall composition of apatite. The main components are CaO (54.83~55.64 wt.%) and P_2O_5 (41.37~42.57 wt.%). The content of F ranges from 1.62 to 2.20 wt.%, consistent with the characteristic F concentrations of igneous apatite (Belousova *et al.*, 2002).

https://doi.org/10.1180/mgm.2025.10155 Published online by Cambridge University Press

Table 1. EPMA analysis of the chemical composition from core to the rim of apatite

Constituent	A1				A2			
	core	→		rim	core	→		rim
wt. %								
P_2O_5	41.37	42.26	42.57	41.98	42.19	42.16	42.07	41.69
SiO_2	0.10	0.12	0.10	0.14	0.09	0.10	0.07	0.08
Nd_2O_3	0.13	0.06	0.08	0.08	0.18	0.16	0.17	0.07
Ce_2O_3	0.20	0.18	0.07	0.08	0.07	0.17	0.06	0.12
La_2O_3	0.00	0.04	0.05	b.d.l	0.09	b.d.l	0.03	0.01
FeO	0.15	0.13	0.09	0.07	0.17	0.15	0.11	0.10
MnO	0.09	0.09	0.10	0.09	0.07	0.14	0.09	0.08
MgO	0.02	0.01	0.03	0.04	0.03	0.01	0.01	0.05
CaO	55.60	55.20	54.99	55.64	55.26	54.83	55.05	55.32
SrO	0.10	0.10	0.10	0.11	0.07	0.02	0.05	0.08
Na_2O	0.03	0.00	0.01	0.03	0.07	0.04	0.01	0.09
SO_3	0.03	0.06	0.03	0.03	0.02	0.03	0.02	0.03
F	2.07	2.17	2.20	2.07	1.62	1.53	1.80	1.76
Cl	0.18	0.19	0.19	0.19	0.20	0.19	0.15	0.19
Total	99.25	99.72	99.64	99.68	99.49	98.85	98.90	98.88
Calculated based on 25 anions (Ketcham, 2015)								
P	2.83	2.86	2.87	2.85	2.89	2.90	2.88	2.86
Si	0.02	0.02	0.02	0.02	0.01	0.00	0.00	0.00
S	0.00	0.01	0.00	0.00	0.00	0.01	0.00	0.00
Ca	9.62	9.44	9.39	9.55	9.57	9.54	9.54	9.63
Nd	0.00	0.00	0.00	0.00	0.01	0.00	0.00	0.01
Ce	0.01	0.01	0.00	0.00	0.00	0.01	0.00	0.00
La	0.00	0.00	0.00	0.00	0.00	0.00	0.00	0.00
Sr	0.01	0.01	0.01	0.01	0.01	0.00	0.00	0.01
Na	0.00	0.00	0.00	0.00	0.01	0.00	0.00	0.01
Mn	0.01	0.01	0.01	0.01	0.01	0.02	0.01	0.01
Fe	0.02	0.02	0.01	0.01	0.02	0.02	0.01	0.01
Mg	0.00	0.00	0.01	0.01	0.01	0.00	0.00	0.01
F	1.06	1.10	1.11	1.05	0.83	0.79	0.92	0.90
Cl	0.05	0.05	0.05	0.05	0.05	0.05	0.04	0.05
OH^*(=2-F-Cl)	0.89	0.85	0.84	0.90	1.12	1.16	1.04	1.05

b.d.l: below the detection limit.

Due to their tiny size, the lath-shaped inclusions cannot be analyzed quantitatively by EPMA. However, the element distribution in the apatite host and inclusions can be assessed through SEM-EDS mapping. The exposed inclusion areas

https://doi.org/10.1180/mgm.2025.10155 Published online by Cambridge University Press

are mainly composed of Fe and O, suggesting the inclusions are iron oxides or iron hydroxides (Fig. 4). Additional EDS mapping for Al, Ti, and Mg did not show significant enrichment within the inclusion regions, suggesting that these elements are either absent or below the detection limit in the inclusions.

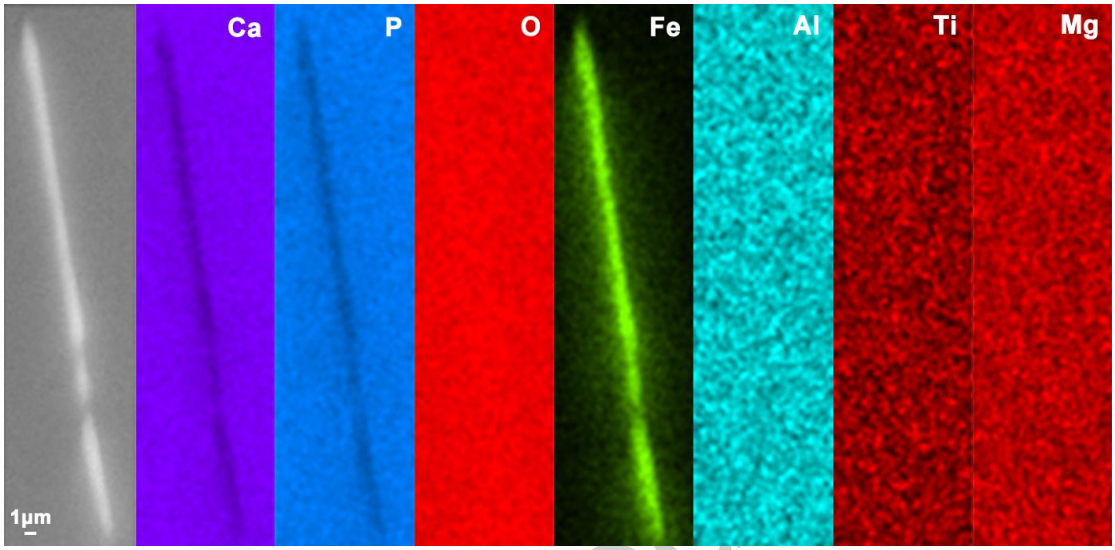

Fig. 4. BSE image and EDS mapping of Ca, P, O, Fe, Al, Ti and Mg of an exposed inclusion area from thin section A1.

Phase identification of inclusions

According to SEM-EDS analysis, the inclusions were identified as iron oxide or iron hydroxides. To further characterize the phase, Raman spectra were obtained from both the host and exposed inclusion regions (Fig. 5). The strongest band at 960 cm^{-1} corresponds to the v_1 PO_4 stretching mode; the v_2 PO_4 mode appears at 430 and 448 cm^{-1}, and the v_4 PO_4 mode is observed at 579, 589 and 605 cm^{-1}; weak bands at 1037, 1046 and 1074 cm^{-1} may correspond to the v_3 PO_4 mode or potentially the v_1 CO_3 mode, while the band at 1156 cm^{-1} is attributed to either the v_1 CO_3 mode or REEs emission within apatite (Antonakos *et al.*, 2007).

The Raman spectrum of iron oxide inclusions displays three additional bands at approximately 662, 528 and 304 cm^{-1}, in addition to those observed for the host apatite. These bands are consistent with the characteristic vibrational modes of magnetite, with the band at 662 cm^{-1} assigned to the A_{1g} mode of magnetite, and those at 528 cm^{-1} and 304 cm^{-1} correspond to the T_{2g} and E_g modes, respectively (Shebanova and Lazor, 2003). For further identification, these vibration bands were

https://doi.org/10.1180/mgm.2025.10155 Published online by Cambridge University Press

compared with other Fe oxides and hydroxides. For iron oxides exist stably at room temperature, hematite generally shows strong vibrational modes at about 226, 299, 410, and 611 cm^{-1}, and maghemite exhibits bands around 350, 500, 660, and 700 cm^{-1} (De Faria *et al.*, 1997). Iron hydroxides, including goethite and lepidocrocite, show main vibrational bands at 299, 479, 550, and 685 cm^{-1} for goethite, and 245, 373, 522, and 650 cm^{-1} for lepidocrocite (De Faria *et al.*, 1997). None of these phases match the precise positions of the observed inclusion spectra in this research. In addition, EDS mapping of the inclusion exposed region reveals only Fe and O, with no detectable signals for other possible relevant elements, such as Al, Mg and Ti, which effectively rules out Fe-Al spinels or Fe-Ti oxides (Fig. 4).

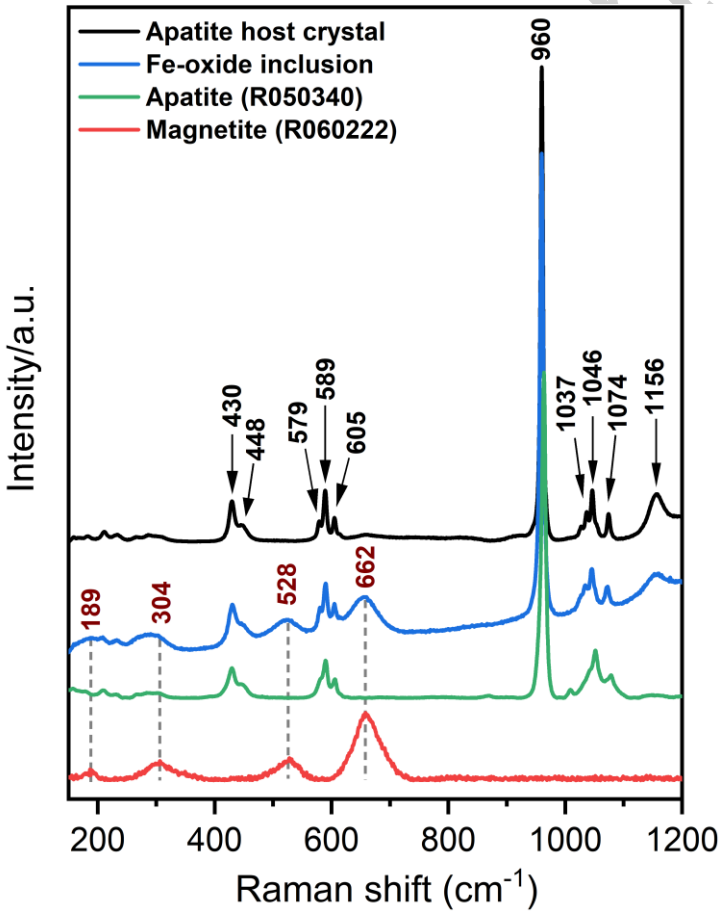

Fig. 5. Raman spectra of host apatite and iron oxide inclusions. The green-line is the standard Raman spectrum of apatite, and the red-line spectrum is the standard Raman spectrum of magnetite from the RRUFF database (https://rruff.info/).

Inclusions other than iron oxides are also identified by Raman spectroscopy. The gaseous phase exhibits characteristic CO_2 vibration modes at 1286 and 1388 cm^{-1}, along with the N_2 vibration mode at 2329 cm^{-1} (Fig. 6a). Compared to the apatite host,

https://doi.org/10.1180/mgm.2025.10155 Published online by Cambridge University Press

the liquid inclusions present Raman bands associated with carbonate (Fig. 6a), with bands observed at 1042, 684 and 145 cm^{-1}, assigned to the v_1, v_4 and the translational mode of the carbonate ion, respectively; additional bands at 1435 and 1458 cm^{-1} are attributed to the carbonate v_3 mode, and the 1622 cm^{-1} band might be related to the carbonate ion within the apatite channel site (Antonakos *et al.*, 2007; Buzgar and Apopei, 2009; Murphy *et al.*, 2021). Raman spectra of the prism-like inclusions (as seen in Fig. 3e) show a carbonate vibration mode, which identified the inclusion as calcite (Fig. 6b).

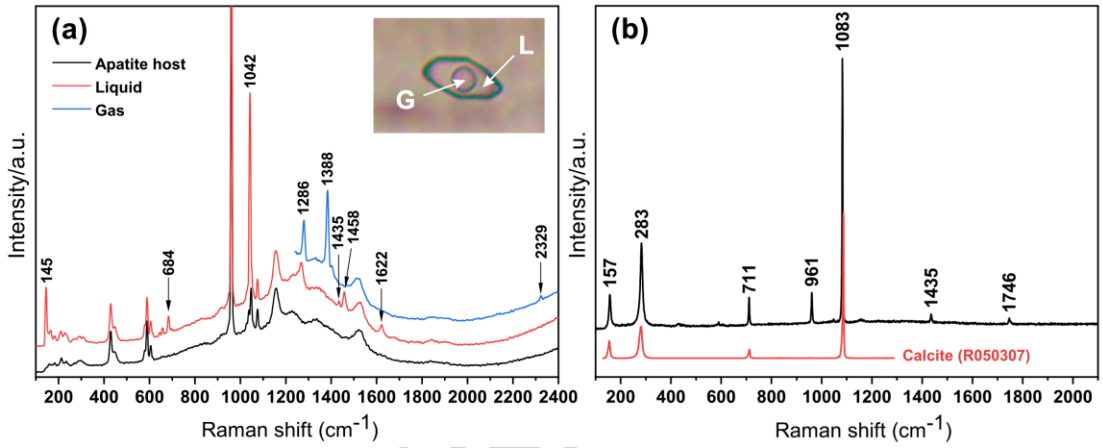

Fig. 6. Raman spectra of (**a**) gas-liquid two-phase inclusions and (**b**) prismatic inclusions in apatite. The standard Raman spectrum of calcite is from the RRUFF database (https://rruff.info/).

Crystallographic and shape orientation relationships

The crystallographic orientation relationship between the host apatite and magnetite inclusions was determined by EBSD analysis, conducted on the exposed areas of inclusion within thin section samples. To improve accuracy, multiple single cross-sectional areas in three different trace directions in the thin section TS-1 were selected for EBSD measurement. Figure 7 presents BSE imaging of thin section A1, showing cross-sections of inclusions in three different shape-preferred orientations, along with electron backscatter diffraction patterns (EBSP) of both apatite and inclusions (Fig. 7). Since similar EBSD pole figures were obtained from samples TS-1 and TS-2, only data from sample TS-1 are presented here to represent the COR and SOR (as Fig. 8).

https://doi.org/10.1180/mgm.2025.10155 Published online by Cambridge University Press

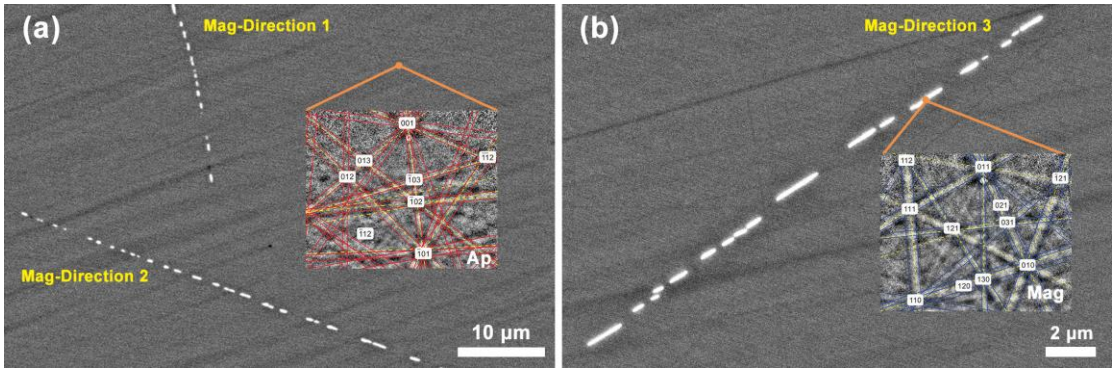

Fig. 7. (**a**) BSE image of sample TS-1, showing the apatite host and magnetite inclusions in direction 1 and 2. The smaller figure on the right is the Kikuchi pattern of apatite. (**b**) Magnetite inclusions in direction 3 on the same thin section. The smaller figure on the right is the Kikuchi pattern of magnetite. All descriptions of magnetite directions correspond to those shown in Fig. 2b.

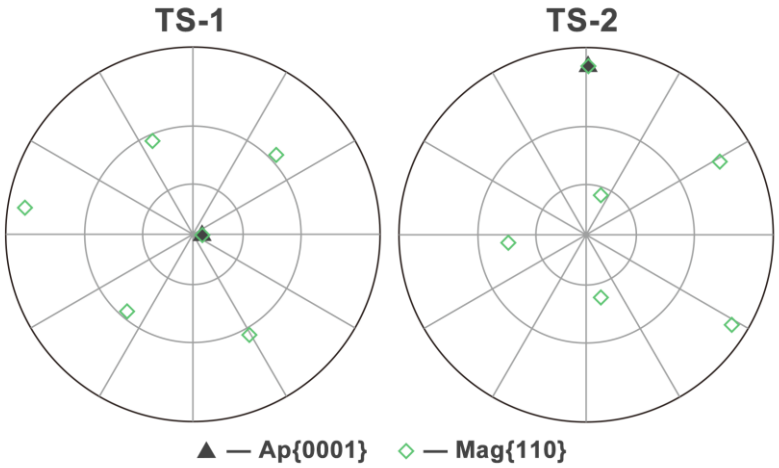

Fig. 8. The pole figures of TS-1 and TS-2, including apatite {0001} and magnetite {110}, indicate that the magnetite inclusions and apatite host have consistent axial relationships in two different samples.

Optical microscopy and pole figures demonstrate the SPO of elongated inclusions aligned parallel to $<11\bar{2}0>$ directions of apatite host (Fig. 9). The crystallographic orientations of apatite and magnetite inclusions were analyzed by using EBSD and plotted as pole figures (Fig. 9a, 9b). In the pole figure of apatite (Fig. 9a), three low-index planes {0001}, $\{10\bar{1}0\}$, and $\{11\bar{2}0\}$ are projected, showing a consistent host orientation across all mapped areas. Regarding the projection poles of magnetite, we found that the crystallographic orientation of inclusions with the same elongation direction was nearly consistent. Inclusions are divided into three SPO directions based on their elongation orientations in TS-1. All magnetite inclusions, regardless of SPO direction, display a common axial orientation relationship of $<0001>_{Ap}//<110>_{Mag}$, as evidenced by the overlap of apatite {0001} and magnetite {110} pole. In addition to the axial relationship $<0001>_{Ap}//<110>_{Mag}$, distinct planar

https://doi.org/10.1180/mgm.2025.10155 Published online by Cambridge University Press

orientation relationships are observed, which defined two specific CORs. COR-1: one of the $\{11\bar{2}0\}_{Ap}$ planes parallel to one of the $\{411\}_{Mag}$ planes, and one of the $\{10\bar{1}0\}_{Ap}$ planes is parallel to one of the $\{211\}_{Mag}$ planes. COR-2: one of the $\{11\bar{2}0\}_{Ap}$ planes parallel to one of the $\{211\}_{Mag}$ planes, and one of the $\{10\bar{1}0\}_{Ap}$ planes is parallel to one of the $\{411\}_{Mag}$ planes. Direction 3 shows the same set of relationship with direction 1, but as a symmetrically equivalent variant, representing the second variant of COR-1 (Fig. 9b). The inverse pole figure (IPF) color maps show that all inclusions share the same color in Z_0 direction (parallel to the apatite c-axis), while in-plane orientations vary between the three directions (Fig. 9c). Direction 1 shows a different IPF color compared to Directions 2 and 3, which exhibit similar colors, indicating similar crystallographic orientations within their respective inclusion groups. For magnetite inclusions in three directions, the poles of directions 2 and 3 have similar but not identical positions (misorientation ca. 5 degrees about the shared $<0001>_{Ap}//<110>_{Mag}$ axis pair), while the poles of direction 1 are rotated around 60 degrees clockwise about the shared $<0001>_{Ap}//<110>_{Mag}$ axis pair relative to the other two directions (Fig. 9b).

https://doi.org/10.1180/mgm.2025.10155 Published online by Cambridge University Press

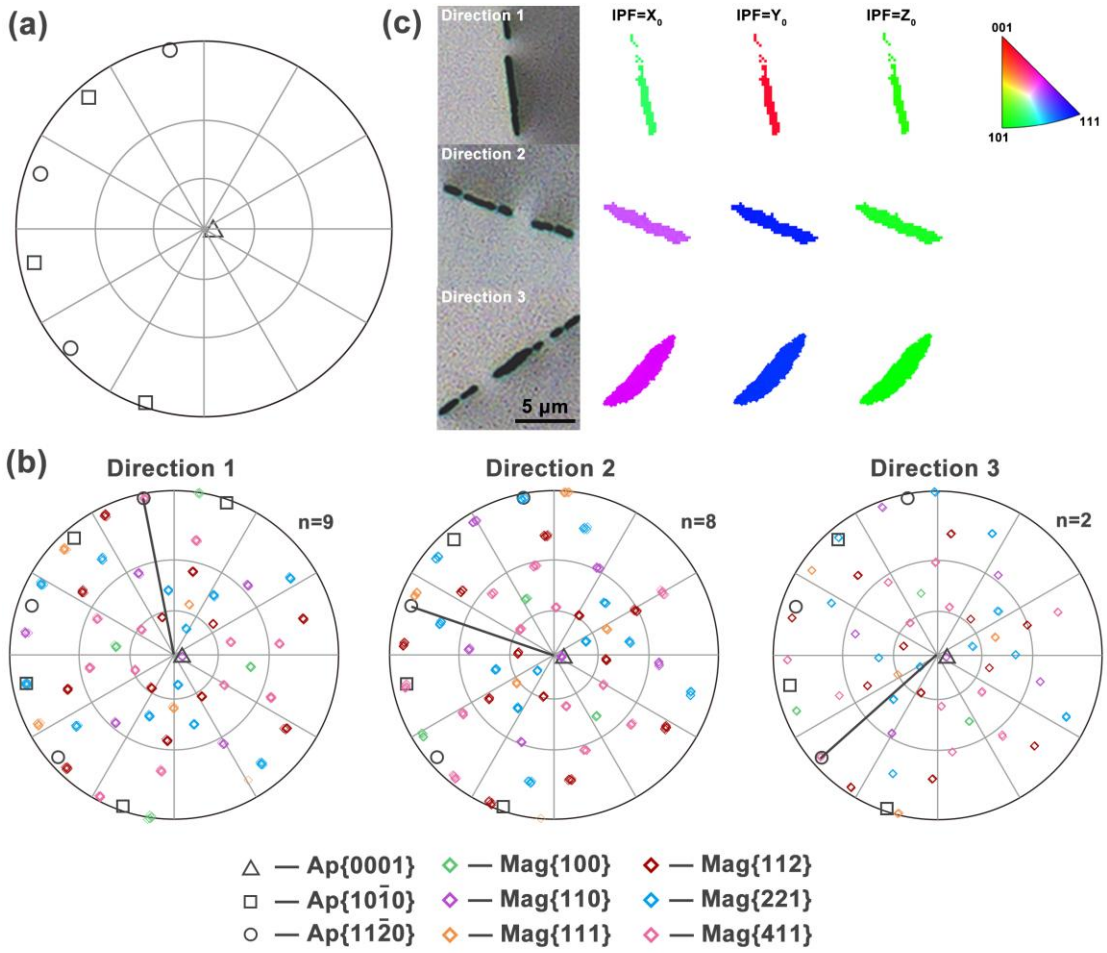

Fig. 9. Shape and crystallographic orientation relationships between magnetite inclusions and apatite host. (**a**) Pole figure of host apatite, showing the three low-index planes {0001}, {10$\bar{1}$0}, and {11$\bar{2}$0}. (**b**) Pole figures of magnetite inclusions in three direction. The index symbols are marked to indicate the main crystallographic orientations of the two phases. The black lines represent the extension of the inclusions in each direction. (**c**) Optical microphotographs and IPF colors of chosen magnetite inclusions in three directions in the thin section TS-1. The IPFs do not represent the actual sizes of the cross section of inclusions. All directional descriptions of magnetite correspond to those shown in Fig. 2b and Fig. 7.

Discussion and Conclusions

SOR and COR between magnetite and apatite

The formation mechanism of shape-preferred mineral inclusions has received extensive attention, and numerous models have been proposed to explain their genesis. Several studies have summarized the following hypotheses so far (Proyer *et al.*, 2013; Axler and Ague, 2015b; Keller and Ague, 2019): 1) overgrowth of pre-crystallized, preferentially oriented minerals that are trapped by later-grown minerals (Spiess *et al.*, 2007); 2) heterogeneous nucleation and co-growth of host and inclusion

https://doi.org/10.1180/mgm.2025.10155 Published online by Cambridge University Press

phases (Hwang *et al.*, 2015; Palke and Breeding, 2017; Griffiths *et al.*, 2020; Kohn *et al.*, 2024); 3) exsolution (Axler and Ague, 2015a; Keller and Ague, 2022); 4) open-system precipitation (OSP) (Proyer *et al.*, 2009; Proyer *et al.*, 2013); 5) inclusions crystallized along cleavage planes or fractures within the host crystal (Hwang *et al.*, 2007a; Hwang *et al.*, 2007b; Hwang *et al.*, 2013); 6) fluid-assisted dissolution-reprecipitation (Harlov *et al.*, 2002; Harlov *et al.*, 2005; Harlov, 2011; Hwang *et al.*, 2019); 7) recrystallization of pre-existing inclusions (Ageeva *et al.*, 2016; Bian *et al.*, 2023), etc. It is noteworthy that in natural geological environments, multiple mechanisms may operate simultaneously during inclusion formation.

When CORs and SORs are observed, they can help to constrain the possible formation processes, although not every mechanism can produce them. CORs are generated from interactions between host and inclusion lattices, reflecting the formation of low energy interfaces, typically resulting in correlations between specific crystallographic directions or planes (Habler and Griffiths, 2017; Griffiths *et al.*, 2020). The nucleation mode of inclusions determines the nature of lattice matching mode between neighboring phases. In three-dimensional lattice matching mode, inclusions nucleate under complete crystallographic control by the host, rather than being confined to a pre-existing interface, and the resulting CORs and SORs are expected to be determined by the alignment of multiple (typically low-index) planes in both phases at interfaces, to minimize the total lattice strain and interfacial energy of the inclusions. In this process, there is no reason to prefer any single symmetrical equivalent variant of a given COR or SOR, so all symmetric equivalents are expected to be equally frequently represented. One representative process is exsolution, in which a supersaturated host undergoes phase separation under sub-solidus conditions due to temperature or pressure changes, without introducing or removing chemical components. For instance, trigonal ilmenite (Ilm) is commonly exsolved from magnetite, and their combination is based on close-packed oxygen atoms, characterized by CORs featuring $<110>_{Mag}//<10\bar{1}0>_{Ilm}$ and $(111)_{Mag}//(0001)_{Ilm}$ (Tan *et al.*, 2016).

By contrast, in a two-dimensional lattice matching mode, nucleation occurs on a

https://doi.org/10.1180/mgm.2025.10155 Published online by Cambridge University Press

pre-existing fixed substrate, such as a specific host facet during heterogeneous nucleation. In this scenario, the growth orientation of the new phase is constrained by the surface structure of the substrate, making the resulting SORs and CORs directly dependent on its crystallography (Griffiths *et al.*, 2020). Because energy minimization is confined to this single interface, the overall symmetry of the host-inclusion system is broken. This creates the potential for the selection of specific, symmetrically equivalent variants of a given COR and/or SOR (Kohn *et al.*, 2024). In these cases of nucleation on a substrate, SPO may develop either simultaneously with host growth or due to post-crystallization re-equilibration of inclusion shape. For instance, Kohn et al. (2024) report a rare SPO pattern in rutile needles within meta-pegmatitic garnet from the Bohemian Massif, attributed to nucleation on the garnet {112} facets. Rutile needles with an SPO following the specific <111> garnet direction lying in the {112} growth facet plane are absent, emphasizing the role of substrate orientation in defining SORs and CORs. And, as demonstrated by Hwang et al. (2013), even regularly oriented inclusions with apparent SPO and CORs may form through interface-controlled or metasomatic processes such as cleavage-controlled precipitation, rather than being directly inherited from co-crystallization with the host (Hwang *et al.*, 2013). In the present study, lamellar magnetite inclusions within apatite are observed to occur in trails parallel to $(10\bar{1}0)$ facets of apatite and exhibit a consistent set of three SPOs, each being aligned parallel to the <0001> axis of apatite and elongated along one of the three $<11\bar{2}0>$ directions of apatite, specifically the one (sub)parallel to the elongation direction of the inclusion trail. This structural configuration already suggests that magnetite nucleation was governed by an interface-controlled mechanism, where inclusion growth was influenced by the crystallographic orientation of the host substrate, rather than by a fully three-dimensional lattice match, otherwise all three SPOs might be expected to occur simultaneously in one trail. However, COR information is required to completely rule out exsolution, as the minor possibility remains that all inclusions in each trail are interconnected (although it should be noted that exsolution does not usually form "skeletal" lamellae).

https://doi.org/10.1180/mgm.2025.10155 Published online by Cambridge University Press

For host-inclusion phases belonging to different crystal systems with disparate lattice parameters, such as apatite and magnetite, growth may proceed along a pair of fpartially fitting directions to minimize interfacial energy, even when ideal lattice matching cannot be achieved. According to the pole figures (Fig. 9b), a fundamental alignment may be established that allows magnetite to nucleate stably on the apatite substrate in the initial stage of nucleation. Pole figure analysis also indicates that one of the magnetite close-packed plane {111} is sub-parallel to one of the principal prism plane of apatite, suggesting these close-packed planes provide a reference framework for the primary alignment. A subsequent, secondary stage of rotational adjustment can refine this relationship to reduce lattice misfit, producing the specific CORs observed. The form of that refinement depends on the SPO: in directions 1 and 3, the initial alignment is a $\{111\}_{Mag}$ sub-parallel to a $\{10\bar{1}0\}_{Ap}$ and evolves into COR-1 (with variants), whereas in direction 2, the alignment of $\{111\}_{Mag}$ sub-parallel to a $\{11\bar{2}0\}_{Ap}$ leads to COR-2. In a fully 3D volume-controlled nucleation, symmetrically equivalent COR variants would be expected to appear with similar frequencies, since orientation would be constrained by minimizing energy across all interfaces bounding the inclusion. However, in our samples, SPO in direction 1 and 3 consistently yield two symmetrically related variants of COR-1, whereas direction 2 exhibits a distinct and unrelated COR-2. This SPO-dependent selection of CORs is difficult to reconcile with a simple 3D volume-controlled nucleation model and instead indicates variant selection by 2D interface-control.

Another noteworthy observation concerns the relationship between the CORs and the actual phase-boundary traces. The planar CORs we identify involve relatively high-index magnetite planes {411} and {211}, paired with low-index prism planes of apatite. Inspection of inclusion cross-section traces (Fig. 7b) shows subtle deviations from exact parallelism with low-index host planes, consistent with the presence of apparently “irrational” interface planes that achieve the interfacial energy minimization. The study by Fleet et al.on oriented magnetite in pyroxene provides a classic model (Fleet *et al.*, 1980), which demonstrated that while the COR is rational, the inclusion boundaries themselves are seemingly irrational orientations to form an

https://doi.org/10.1180/mgm.2025.10155 Published online by Cambridge University Press

optimal phase boundary that minimizes lattice strain. While such interfaces are clear evidence of energy minimization, they can arise by various mechanisms, including both 2D interface-controlled and 3D volume-controlled nucleation modes (Peres et al., 2024). The critical evidence for interface-control in our samples comes from the patterned selection of COR variants according to SPO, together with the axial alignment and the observed boundary-trace mismatches. These features indicate that the system minimized energy at specific nucleation interfaces in a manner controlled by the local substrate geometry. Such a pattern is not expected for a 3D volume-controlled mechanism, which would impose a single averaged COR. On this basis, we infer that the magnetite inclusions formed predominantly through 2D interface-controlled nucleation on specific apatite substrate facets, while acknowledging that mixed or alternative mechanisms cannot be entirely excluded.

Formation of magnetite inclusions in apatite

Magnetite micro-inclusions exhibiting SPO are commonly observed in plagioclase and clinopyroxene, as described in several studies (Fleet *et al.*, 1980; Feinberg *et al.*, 2004; Wenk *et al.*, 2011; Ageeva *et al.*, 2016; Ageeva *et al.*, 2022; Jin *et al.*, 2022; Bian *et al.*, 2023). The genesis of these inclusions is complex; multiple generations can coexist within a single host crystal, ranging from needle-like inclusions formed by early-stage exsolution to lath-shaped or discontinuous inclusions resulting from coarsening and dissolution during late-stage hydrothermal processes (Ageeva *et al.*, 2016; Ageeva *et al.*, 2017; Bian *et al.*, 2023). In most mechanisms, the constituent elements of the inclusions are derived from the host mineral itself, such as through exsolution and OSP, including the needle-shaped magnetite inclusions with specific CORs in plagioclase or clinopyroxene mentioned above. However, in the case of this study, Fe is less likely to be stored in the apatite host before the formation of magnetite inclusions. The cation sites in apatite have a low capacity to accommodate Fe ions and only a small amount can substitute for calcium ions (Pan and Fleet, 2002). According to EPMA analysis, the range of FeO is 0.07~0.17%, indicating a low Fe content in the apatite structure. The observed SPO and CORs of the host-inclusion

https://doi.org/10.1180/mgm.2025.10155 Published online by Cambridge University Press

system also suggest that Fe is not exsolved from the apatite lattice. Oppositely, these observations suggest that the Fe was introduced from an external source, either during the crystallization of apatite from melt or fluid, or possibly through fluid infiltration after the apatite had formed.

When excluding the possibility of Fe exsolved from the apatite lattice, we propose an alternative mechanism in which Fe diffuse into the apatite structure and subsequently nucleate into magnetite at favorable sites. The apatite crystal structure presents nano-channels parallel to the c-axis, typically occupied by F^-, Cl^-, or OH^- anions, which may facilitate such diffusion pathways. Meanwhile, anions with different valence states, certain transition metal ions, and vacancies can exist in the channel as additional substituents (Pan and Fleet, 2002). With the assistance of aqueous fluid with a certain salinity, cations can diffuse into apatite through these nano-channels, which provide sites for nucleation and growth (Harlov *et al.*, 2005). This mechanism allows a significant amount of Fe to diffuse into the host.

A comparable mechanism has been proposed for the formation of oriented magnetite inclusions in plagioclase. The Si-Al-O tetrahedral framework of plagioclase forms channels parallel to [001], which are thought to accommodate the diffusion of Fe-bearing species. Within these structural pathways, iron may be incorporated and subsequently form FeO_6 octahedra (Wenk *et al.*, 2011; Ageeva *et al.*, 2020). Oriented pyrrhotite and triphylite in apatite have been attributed to this mechanism (Broska *et al.*, 2014; Kurylo *et al.*, 2025). In laboratory, Fe-containing apatite-type solid solutions have been synthesized by diffusing Fe into the channel sites of apatite (Kato *et al.*, 2018). However, inclusions in the above cases are only elongated along the c-axis of apatite and do not exhibit any SPO parallel to $<11\bar{2}0>$ directions. Therefore, other possible situations should be considered.

Apatite is commonly dissolved by fluids in the natural environment, with dissolution surfaces controlled by the crystallographic structure of apatite itself, resulting in the formation of etch pits on external crystal facets. Generally, hexagonal etch pits with $(10\bar{1}0)$ walls can be observed on the basal pinacoid of apatite (Fig. 10) (Rakovan, 2002). In acid solutions (especially at pH<3), hexagonal etch pits also form

https://doi.org/10.1180/mgm.2025.10155 Published online by Cambridge University Press

linear etch grooves extending along the <11$\bar{2}$0> directions of apatite, suggesting that this is a weakly bonded orientation in the apatite crystal structure (Rakovan and Reeder, 1994; Tseng *et al.*, 2006). Thirioux et al. observed that, in acid environment, apatite also presents trapezoidal etch pits on (10$\bar{1}$0), which anisotropically expand along <0001> as dissolution continues, to form etch grooves (Fig. 10a) (Thirioux *et al.*, 1990). In addition, hillocks can be observed on the (0001) basal pinacoid of natural apatite and growth spirals are frequently observed on (10$\bar{1}$0) prism facets (Thirioux *et al.*, 1990). These features, developing on crystal structure defects such as dislocations, can serve as seeds for crystal growth and promote growth on smooth interfaces (Amelinckx, 1952; Rakovan, 2002). Free elements can also be preferentially adsorbed at crystal defects such as dislocations or surface microstructures generated by dissolution and may subsequently diffuse to energetically favorable sites for nucleation.

On the basal pinacoid of the euhedral sample A1 in this study, abundant hexagonal etch pits were observed, with some larger pits aligned along the <11$\bar{2}$0> direction of apatite (Fig. 10b and 10c). These etch pits exhibit the same orientation as the magnetite inclusion trails observed in thin section TS-1, which was cut parallel to the basal pinacoid. The spatial correspondence suggests that the formation of magnetite inclusions may be linked to the hexagonal etch pits. Based on the crystal structure of apatite and optical microscopy observations, we propose that Fe-bearing fluids entered the crystal through etch pits, where they interacted with channels extending along the [0001] direction on {10$\bar{1}$0} facets. These structural features may serve as preferential nucleation sites, promoting interface-controlled nucleation of magnetite inclusions with a shape-preferred orientation aligned with [0001] of apatite. Correspondingly, the inclusions exhibit trapezoidal shapes parallel to (10 $\bar{1}$ 0), matching the geometry of etch pits observed on this facet (Fig. 2e). The alignment of inclusion trails along <11 $\bar{2}$ 0> suggests it is one of the preferred directions for dissolution, potentially facilitated by the acidity of the fluid. In addition, the basal pinacoid facets may also act as initiation sites, generating dissolution channels elongated parallel to <0001> of apatite at the same time. While the inclusions appear

https://doi.org/10.1180/mgm.2025.10155 Published online by Cambridge University Press

discontinuous in cross-section, EBSD mapping shows that inclusions within a single trail consistently share the same crystallographic orientation, indicating that they are either structurally connected or derived from a common orientation variant, established through interfacial crystallographic control during nucleation. One possibility is that inclusions nucleated independently at different points along each channel but adopted a uniform orientation due to strong crystallographic control at the interface. In this case, the discontinuous appearance of magnetite in section TS-1 could reflect the initial presence of small, isolated inclusions nucleated within discrete etch pits. As the solution front advanced and the affected zone widened, these inclusions may have coarsened and become structurally connected, as suggested by observations in Fig. 2c and 2e. Alternatively, they may represent a single, continuous lamella that grew progressively during apatite dissolution. Or, these discrete inclusions may have been formed by fluid erosion of a thin sheet, but because they were originally a single entity, the elongated inclusions retain a consistent crystal orientation.

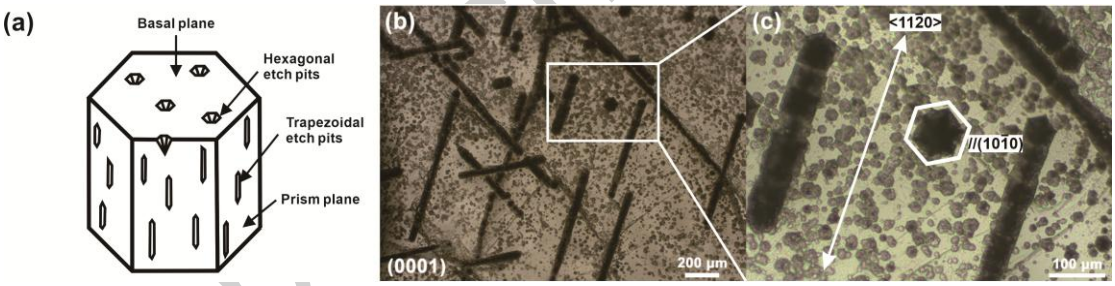

Fig. 10. (**a**) Typical dissolution features on crystal facets of apatite. After Thirioux et al. (1990). (**b**) Continuous etching pits observed on the basal pinacoid of euhedral sample A1. (**c**) Further magnified observation shows the hexagonal shape of single pit, and the sides of hexagon are parallel to the $\{10\bar{1}0\}$ prism facets of apatite. The etching pits arranging continuously along the $<11\bar{2}0>$ directions of apatite.

In the natural environment, apatite is widely distributed and generally undergoes a complex history of hydrothermal overprint and metasomatic alteration. The abundant gas-liquid inclusions in the analyzed samples indicate a history of fluid infiltration, while the coexistence of CO_2 and N_2 in the gaseous phase, along with carbonate ions in the liquid phase, suggests the involvement of volatile-rich, mildly acidic fluids. A lot of them also display a necking-down appearance, implying the host apatite crystal had gone through a dissolution-recrystallization process. Under

https://doi.org/10.1180/mgm.2025.10155 Published online by Cambridge University Press

extensive metasomatic alteration, compositional zoning is commonly observed in apatite, as shown in natural and experimental cases involving oriented monazite inclusions that withdraw REEs from the apatite lattice (Harlov *et al.*, 2005). In F-Cl-SO_2-P-rich fluids, P and REEs tend to be leached from apatite (Harlov *et al.*, 2002), whereas in CO_2-K-Cl-rich fluids, the mobility of these elements is significantly reduced (Bonyadi *et al.*, 2011). In our apatite samples, however, EPMA analysis reveals a relatively homogeneous chemical composition, and BSE imaging shows no contrast differences around magnetite inclusions, indicating an absence of compositional zoning. Therefore, the altering fluid is inferred to correspond to the characteristics of a Fe-CO_2-rich aqueous fluid, with no clear evidence for the presence of other significant elemental components.

Previous studies on carbonatite-related apatite have documented oriented Fe-rich inclusions, primarily pyrrhotite, indicating a carbonate-sulfate-dominated fluid environment (Broska *et al.*, 2014; Hurai *et al.*, 2017). In contrast, the Fe-related inclusions in our samples are exclusively oxides, and the sulfur content in the host apatite is limited. This implies low sulfur activity in the fluid system, potentially distinguishing these apatites from typical carbonatite-associated deposits.

In conclusion, this study provides new insights on the chemical composition and the inclusion phase content within the studied apatite, as well as the crystallographic orientation relationships between host apatite and magnetite inclusions. However, several questions remain unresolved. As the samples are found from a secondary deposit, and both apatite and magnetite can crystallize over a broad temperature range, it is difficult to constrain the origin of Fe based on its original geological context. Apatite samples with surrounding minerals are needed for further analysis.

https://doi.org/10.1180/mgm.2025.10155 Published online by Cambridge University Press

Reference

Ageeva O., Bian G., Habler G., Pertsev A. and Abart R. (2020) Crystallographic and shape orientations of magnetite micro-inclusions in plagioclase. *Contributions to Mineralogy and Petrology*, **175**, 1-16.

Ageeva O., Habler G., Gilder S.A., Schuster R., Pertsev A., Pilipenko O., Bian G. and Abart R. (2022) Oriented magnetite inclusions in plagioclase: Implications for the anisotropy of magnetic remanence. *Geochemistry, Geophysics, Geosystems*, **23**, e2021GC010272.

Ageeva O., Habler G., Pertsev A. and Abart R. (2017) Fe-Ti oxide micro-inclusions in clinopyroxene of oceanic gabbro: Phase content, orientation relations and petrogenetic implication. *Lithos*, **290**, 104-115.

Ageeva O., Habler G., Topa D., Waitz T., Li C., Pertsev A., Griffiths T., Zhilicheva O. and Abart R. (2016) Plagioclase hosted Fe-Ti-oxide micro-inclusions in an oceanic gabbro-plagiogranite association from the Mid Atlantic Ridge at 13°34'N. *American Journal of Science*, **316**, 85-109.

Amelinckx S. (1952) Spiral growth patterns on apatite crystals. *Nature*, **169**, 841-842.

Antonakos A., Liarokapis E. and Leventouri T. (2007) Micro-Raman and FTIR studies of synthetic and natural apatites. *Biomaterials*, **28**, 3043-3054.

Ashley K.T., Darling R.S., Bodnar R.J. and Law R.D. (2015) Significance of "stretched" mineral inclusions for reconstructing P-T exhumation history. *Contributions to Mineralogy and Petrology*, **169**, 1-9.

Axler J.A. and Ague J.J. (2015a) Exsolution of rutile or apatite precipitates surrounding ruptured inclusions in garnet from UHT and UHP rocks. *Journal of Metamorphic Geology*, **33**, 829-848.

-. (2015b) Oriented multiphase needles in garnet from ultrahigh-temperature granulites, Connecticut, USA. *American Mineralogist*, **100**, 2254-2271.

Barot N., Graziani G., Gübelin E. and Rettighieri M. (1995) Cat's-eye and asteriated gemstones from East Africa. *Journal of Gemmology*, **24**, 569-580.

Belousova E., Griffin W., O'Reilly S.Y. and Fisher N. (2002) Apatite as an indicator mineral for mineral exploration: Trace-element compositions and their relationship to host rock type. *Journal of Geochemical Exploration*, **76**, 45-69.

Bian G., Ageeva O., Roddatis V., Habler G., Schreiber A. and Abart R. (2023) Oriented secondary magnetite micro-inclusions in plagioclase from oceanic gabbro. *American Mineralogist*, **108**, 1642-1657.

Bonyadi Z., Davidson G.J., Mehrabi B., Meffre S. and Ghazban F. (2011) Significance of apatite REE depletion and monazite inclusions in the brecciated Se-Chahun iron oxide-apatite deposit, Bafq district, Iran: insights from paragenesis and geochemistry. *Chemical Geology*, **281**, 253-269.

Britton T., Jiang J., Guo Y., Vilalta-Clemente A., Wallis D., Hansen L., Winkelmann A. and Wilkinson A. (2016) Tutorial: Crystal orientations and EBSD—Or which way is up? *Materials Characterization*, **117**, 113-126.

Broska I., Krogh Ravna E.J., Vojtko P., Janák M., Konečný P., Pentrák M., Bačík P., Luptáková J. and Kullerud K. (2014) Oriented inclusions in apatite in a post-UHP fluid-mediated regime (Tromsø Nappe, Norway). *European Journal of Mineralogy*, **26**, 623-634.

Buzgar N. and Apopei A.I. (2009) The Raman study of certain carbonates. *Geologie Tomul L*, **2**, 97-112.

De Faria D.L., Venâncio Silva S. and de Oliveira M.T. (1997) Raman microspectroscopy of some iron

https://doi.org/10.1180/mgm.2025.10155 Published online by Cambridge University Press

oxides and oxyhydroxides. *Journal of Raman Spectroscopy*, **28**, 873-878.

Feinberg J.M., Wenk H.-R., Renne P.R. and Scott G.R. (2004) Epitaxial relationships of clinopyroxene-hosted magnetite determined using electron backscatter diffraction (EBSD) technique. *American Mineralogist*, **89**, 462-466.

Fleet M., Bilcox G.A. and Barnett R.L. (1980) Oriented magnetite inclusions in pyroxenes from the Grenville Province. *The Canadian Mineralogist*, **18**, 89-99.

Griffiths T.A., Habler G. and Abart R. (2016) Crystallographic orientation relationships in host-inclusion systems: New insights from large EBSD data sets. *American Mineralogist*, **101**, 690-705.

-. (2020) Determining the origin of inclusions in garnet: Challenges and new diagnostic criteria. *American Journal of Science*, **320**, 753-789.

Habler G. and Griffiths T. (2017) Crystallographic orientation relationships. Pp. 541-585. In W. Heinrich, and R. Abart, Eds. *Mineral reaction kinetics: Microstructures, textures, chemical and isotopic signatures*, 16, European Mineralogical Union and the Mineralogical Society of Great Britain and Ireland.

Harlov D.E. (2011) Formation of monazite and xenotime inclusions in fluorapatite megacrysts, Gloserheia Granite Pegmatite, Froland, Bamble Sector, southern Norway. *Mineralogy and Petrology*, **102**, 77-86.

Harlov D.E., Andersson U.B., Förster H.-J., Nyström J.O., Dulski P. and Broman C. (2002) Apatite-monazite relations in the Kiirunavaara magnetite-apatite ore, northern Sweden. *Chemical Geology*, **191**, 47-72.

Harlov D.E., Wirth R. and Förster H.-J. (2005) An experimental study of dissolution-reprecipitation in fluorapatite: Fluid infiltration and the formation of monazite. *Contributions to Mineralogy and Petrology*, **150**, 268-286.

Hughes J.M., Cameron M. and Mariano A.N. (1991) Rare-earth-element ordering and structural variations in natural rare-earth-bearing apatites. *American Mineralogist*, **76**, 1165-1173.

Hurai V., Paquette J.-L., Huraiová M., Slobodník M., Hvožďara P., Siegfried P., Gajdošová M. and Milovská S. (2017) New insights into the origin of the Evate apatite-iron oxide-carbonate deposit, Northeastern Mozambique, constrained by mineralogy, textures, thermochronometry, and fluid inclusions. *Ore Geology Reviews*, **80**, 1072-1091.

Hwang S., Shen P., Chu H., Yui T. and Iizuka Y. (2013) A TEM study of the oriented orthopyroxene and forsterite inclusions in garnet from Otrøy garnet peridotite, WGR, Norway: New insights on crystallographic characteristics and growth energetics of exsolved pyroxene in relict majoritic garnet. *Journal of Metamorphic Geology*, **31**, 113-130.

Hwang S., Shen P., Yui T. and Chu H. (2007a) TiO_2 nanoparticle trails in garnet: Implications of inclusion pressure-induced microcracks and spontaneous metamorphic-reaction healing during exhumation. *Journal of Metamorphic Geology*, **25**, 451-460.

Hwang S., Yui T., Chu H., Shen P., Schertl H., Zhang R. and Liou J. (2007b) On the origin of oriented rutile needles in garnet from UHP eclogites. *Journal of Metamorphic Geology*, **25**, 349-362.

Hwang S.L., Shen P., Chu H.T., Yui T.F. and Iizuka Y. (2015) Origin of rutile needles in star garnet and implications for interpretation of inclusion textures in ultrahigh-pressure metamorphic rocks. *Journal of Metamorphic Geology*, **33**, 249-272.

Hwang S.L., Shen P., Chu H.T., Yui T.F., Iizuka Y. and Schertl H.P. (2019) Rutile inclusions in garnet from a dissolution-reprecipitation mechanism. *Journal of Metamorphic Geology*, **37**, 1079-

https://doi.org/10.1180/mgm.2025.10155 Published online by Cambridge University Press

1098.

Jin S., Sun Z. and Palke A.C. (2022) Iron oxide inclusions and exsolution textures of rainbow lattice sunstone. *European Journal of Mineralogy*, **34**, 183-200.

Johnson C. (2014) Cat's-eye apatite from Namibia. *Journal of Gemmology*, **34**, 191.

Kammerling R. and Koivula J. (1990) Greenish-blue cat's-eye apatite. *Gems & Gemology*, **26**, 230.

Kammerling R., Koivula J., Johnson M. and Fritsch E. (1995) Cat's-eye apatites from Madagascar. *Gems & Gemology*, **31**, 205-206.

Kato S., Ikeda S., Saito K. and Ogasawara M. (2018) Fe incorporation into hydroxyapatite channels by Fe loading and post-annealing. *Journal of Solid State Chemistry*, **265**, 411-416.

Keller D.S. and Ague J.J. (2019) Crystallographic and textural evidence for precipitation of rutile, ilmenite, corundum, and apatite lamellae from garnet. *American Mineralogist*, **104**, 980-995.

-. (2022) Predicting and explaining crystallographic orientation relationships of exsolved precipitates in garnet using the edge-to-edge matching model. *Journal of Metamorphic Geology*, **40**, 1189-1218.

Ketcham R.A. (2015) Calculation of stoichiometry from EMP data for apatite and other phases with mixing on monovalent anion sites. *American Mineralogist*, **100**, 1620-1623.

Kohn V., Griffiths T.A., Alifirova T., Daneu N., Ageeva O., Abart R. and Habler G. (2024) Variations in orientation relationships between rutile inclusions and garnet host relate to magmatic growth zoning. *Contributions to Mineralogy and Petrology*, **179**, 69.

Kurylo S., Broska I. and Reto G. (2025) Oriented triphylite rods in apatite from an LCT pegmatite in the Stankuvatske Li-ore deposit, Ukraine: Implications for Li mobility. *American Mineralogist*, **110**, 255-271.

Mauthner M. and Ottaway T. (2015) Gem apatite localities. *Rocks & Minerals*, **90**, 260-269.

Murphy A.E., Jakubek R.S., Steele A., Fries M.D. and Glamoclija M. (2021) Raman spectroscopy provides insight into carbonate rock fabric based on calcite and dolomite crystal orientation. *Journal of Raman Spectroscopy*, **52**, 1155-1166.

Palke A. and Breeding C.M. (2017) The origin of needle-like rutile inclusions in natural gem corundum: A combined EPMA, LA-ICP-MS, and nanoSIMS investigation. *American Mineralogist*, **102**, 1451-1461.

Pan Y. and Fleet M.E. (2002) Compositions of the apatite-group minerals: substitution mechanisms and controlling factors. *Reviews in Mineralogy and Geochemistry*, **48**, 13-49.

Proyer A., Habler G., Abart R., Wirth R., Krenn K. and Hoinkes G. (2013) TiO_2 exsolution from garnet by open-system precipitation: Evidence from crystallographic and shape preferred orientation of rutile inclusions. *Contributions to Mineralogy and Petrology*, **166**, 211-234.

Proyer A., Krenn K. and Hoinkes G. (2009) Oriented precipitates of quartz and amphibole in clinopyroxene of metabasites from the Greek Rhodope: A product of open system precipitation during eclogite-granulite-amphibolite transition. *Journal of Metamorphic Geology*, **27**, 639-654.

Rakovan J. (2002) Growth and surface properties of apatite. *Reviews in Mineralogy and Geochemistry*, **48**, 51-86.

Rakovan J. and Laurs B.M. (2016) Large cat's-eye apatite from Madagascar. *Journal of Gemmology*, **35**, 186-189.

Rakovan J. and Reeder R.J. (1994) Differential incorporation of trace elements and dissymmetrization in apatite: The role of surface structure during growth. *American Mineralogist*, **79**, 892-903.

Schmetzer D., Kiefert D. and Hänni P. (2004) Asterism in beryl, aquamarine and emerald—An update.

https://doi.org/10.1180/mgm.2025.10155 Published online by Cambridge University Press

Journal of Gemmology, **29**, 65-71.

Schmetzer K., Bernhardt H.-J. and Gilg H.A. (2016) Characterization of oriented inclusions in cat's-eye, star and other chrysoberyls. *Journal of Gemmology*, **35**, 28-54.

Schmetzer K., Bernhardt H.-J. and Kiefert L. (2002) Star garnets and star garnet cat's-eyes from Ambatondrazaka, Madagascar. *Journal of Gemmology*, **28**, 13-24.

Shebanova O.N. and Lazor P. (2003) Raman spectroscopic study of magnetite ($FeFe_2O_4$): A new assignment for the vibrational spectrum. *Journal of Solid State Chemistry*, **174**, 424-430.

Spiess R., Groppo C. and Compagnoni R. (2007) When epitaxy controls garnet growth. *Journal of Metamorphic Geology*, **25**, 439-450.

Sun X., Tang Q., Sun W., Xu L., Zhai W., Liang J., Liang Y., Shen K., Zhang Z. and Zhou B. (2007) Monazite, iron oxide and barite exsolutions in apatite aggregates from CCSD drillhole eclogites and their geological implications. *Geochimica et Cosmochimica Acta*, **71**, 2896-2905.

Tan W., He H., Wang C.Y., Dong H., Liang X. and Zhu J. (2016) Magnetite exsolution in ilmenite from the Fe-Ti oxide gabbro in the Xinjie intrusion (SW China) and sources of unusually strong remnant magnetization. *American Mineralogist*, **101**, 2759-2767.

Thirioux L., Baillif P., Touray J.C. and Ildefonse J.P. (1990) Surface reactions during fluorapatite dissolution-recrystallization in acid media (hydrochloric and citric acids). *Geochimica et Cosmochimica Acta*, **54**, 1969-1977.

Tseng W.J., Lin C.C., Shen P.W. and Shen P. (2006) Directional/acidic dissolution kinetics of (OH, F, Cl)-bearing apatite. *Journal of Biomedical Materials Research Part A*, **76**, 753-764.

Wechsler B.A., Lindsley D.H. and Prewitt C.T. (1984) Crystal structure and cation distribution in titanomagnetites ($Fe_{3-x}Ti_xO_4$). *American Mineralogist*, **69**, 754-770.

Wenk H.-R., Chen K. and Smith R. (2011) Morphology and microstructure of magnetite and ilmenite inclusions in plagioclase from Adirondack anorthositic gneiss. *American Mineralogist*, **96**, 1316-1324.

Xu C., Zhao S., Zhou J., He X. and Xu H. (2020) Crystallographic orientation of ilmenite inclusions in amphibole-an electron backscatter diffraction study. *Zeitschrift für Kristallographie-Crystalline Materials*, **235**, 105-116.

Yu J., He X. and Lu Z. (2019) Cause analysis of chatoyancy of sapphires from Shandong, China. *RSC Advances*, **9**, 24420-24427.

Zhang R. and Liou J. (1999) Exsolution lamellae in minerals from ultrahigh-pressure rocks. *International Geology Review*, **41**, 981-993.

https://doi.org/10.1180/mgm.2025.10155 Published online by Cambridge University Press